REFERENCES AND NOTES

1. E. K. Wilson, *Chem. Eng. News* 33 (24 February 1997); G. Taubes, *Science* **275**, 1420 (1997); D. N. Beratan, S. Priyadarshy, S. M. Risser, *Chem. Biol.* **4**, 3 (1997).
2. M. R. Arkin *et al.*, *Science* **273**, 475 (1996).
3. C. J. Murphy *et al.*, *ibid.* **262**, 1025 (1993).
4. D. B. Hall, R. E. Holmlin, J. K. Barton, *Nature* **382**, 731 (1996).
5. P. J. Dandliker, R. E. Holmlin, J. K. Barton, *Science* **275**, 1465 (1997).
6. A. M. Brun and A. Harriman, *J. Am. Chem. Soc.* **114**, 3656 (1992).
7. E. J. C. Olson, D. Hu, A. Hörmann, P. F. Barbara, *J. Phys. Chem. B* **101**, 299 (1997).
8. P. Lincoln, E. Tuite, B. Nordén, *J. Am. Chem. Soc.* **119**, 1454 (1997).
9. S. Priyadarshy, S. M. Risser, D. N. Beratan, *J. Phys. Chem.* **100**, 17678 (1996).
10. R. L. Letsinger and T. Wu, *J. Am. Chem. Soc.* **117**, 7323 (1995).
11. D. H. Waldeck, *Chem. Rev.* **91**, 415 (1991).
12. T. Shida, *Electronic Absorption Spectra of Radical Ions* (Elsevier, Amsterdam, 1988).
13. The hairpin structures were calculated with a modified molecular mechanics (MM2) force field within Hyperchem V5.01 (Hypercube, Waterloo, Ontario).
14. K. M. Guckian *et al.*, *J. Am. Chem. Soc.* **118**, 8182 (1996).
15. F. D. Lewis *et al.*, *ibid.* **117**, 8785 (1995).
16. Fluorescence decays were determined by means of a Photon Technology International Model LS1 photon-counting apparatus with a minimum time resolution of ~0.3 ns.
17. The samples were contained in a 2-mm path length cuvette and had absorbances of about 0.1 at 340 nm. An amplified Ti-sapphire–based laser system was used to pump an optical parametric amplifier to generate ~300-fs, 680-nm pulses (frequency doubled with a potassium dihydrogen phosphate crystal to obtain 340-nm pulses) at a 1.36-kHz repetition rate. Samples were excited with 100 nJ of 340-nm light focused to a 250-μm spot. Absolute transient absorption changes were on the order of 0.01. The uncertainty of the kinetic data increases in the nanosecond regime. For a description of the laser system, see S. R. Greenfield, W. A. Svec, D. Gosztola, M. R. Wasielewski, *J. Am. Chem. Soc.* **118**, 6767 (1996); S. R. Greenfield and M. R. Wasielewski, *Opt. Lett.* **20**, 1394 (1995).
18. The stilbenedicarboxamide singlet state reduction potential is estimated to be ~1.5 V from the sum of its singlet energy (3.4 V) and reduction potential in dimethyl sulfoxide solution [−1.9 V versus standard calomel electrode (SCE)] (*15*). The oxidation potential of dimethylaniline is 0.78 V versus SCE [D. Rehm and A. Weller, *Isr. J. Chem.* **8**, 259 (1970)].
19. N. Mataga, S. Nishikawa, T. Asahi, T. Okada, *J. Phys. Chem.* **94**, 1443 (1990).
20. S. Steenken and S. V. Jovanovic, *J. Am. Chem. Soc.* **119**, 617 (1997).
21. L. P. Candeias and S. Steenken, *ibid.* **111**, 1094 (1989).
22. J. B. Birks, *Photophysics of Aromatic Molecules* (Wiley-Interscience, London, 1970), p. 128.

23. Supported by the Division of Chemical Sciences, Office of Basic Energy Sciences, U. S. Department of Energy, under contracts DE-FG02-96ER14604 (to F.D.L.) and W-31-109-ENG-38 (to M.R.W.). We thank J.-S. Yang for the measurement of fluorescence decays.

7 April 1997; accepted 5 June 1997

Evidence for Interacting Gas Flows and an Extended Volatile Source Distribution in the Coma of Comet C/1996 B2 (Hyakutake)

Walter M. Harris,* Michael R. Combi, R. Kent Honeycutt, Béatrice E. A. Mueller, Frank Scherb

Images of comet C/1996 B2 (Hyakutake) taken during its close approach to Earth show differences in the distribution of gas and dust in the inner coma and reveal two arc-shaped molecular resonant emission features. The morphology of these features, as well as the apparent decoupling gas from dust in the inner coma, suggest that an extended region of icy grains surrounds the nucleus of Hyakutake and contributes substantially to the production of volatiles. Model simulations suggest the same conclusion and indicate that the brighter arc is explainable by the presence of a trailing condensation of ice-bearing granules with a rate of volatile production approximately 23 percent of that of the nucleus.

The approach of comet C/1996 B2 (Hyakutake) to within 0.102 astronomical units (AU) (*1*) of Earth provided ground-based observers with an opportunity to monitor the characteristics of the extreme inner coma of an active comet. Such close encounters with comets are relatively rare, and recent opportunities to study small-scale (≤100 km) structures near comet nuclei have been limited except for the IRAS-Araki-Alcock (C/1983d) apparition and the Giotto and Vega fly-by encounters with 1P/Halley in 1986 (*2–4*). We report on the results of observations performed at the 3.5-m WIYN (*5*) telescope on 26 March 1996, using narrow-band filters (*6*) to image the structure and evolution of different small-scale gas and dust structures within 3.5 arc min (~16,000 km) of Hyakutake's nucleus over 7 hours. These images reveal differences in the radial intensity fall-off and the relative spherical distributions of gas and dust emissions in the inner coma, and show a pair of low-contrast arc-shaped emission features located antisunward of the nucleus (Fig. 1).

Hyakutake was 0.107 AU (*1*) from Earth on 26 March, and this corresponds to 77 km/arc sec, or 15.4 km/pixel in our images. Observations occurred between 5:15 to 12:45 universal time (UT), which was slightly longer than the 6-hour, 14-min rotation period of the nucleus (*7*). We alternated imaging sequences between two filters that isolated either dust at 4850 Å (*6*) or resonant emission of the [$B^2\Sigma^+ - X^2\Sigma^+$, $\Delta\nu = 0$] CN band between 3845 and 3883 Å (*8*). The continuum and CN images were taken 360 s apart to facilitate subtraction of dust emission in the CN filter bandpass. The CN and continuum sequences were interrupted at 8:10 UT for an observation of OH [$A^2\Sigma^+ - X^2\Pi_i$, 0-0; 1-1] emission at wavelengths between 3064 and 3115 Å (*8*). After standard processing (*9*), each image was spatially filtered to emphasize small-scale structures, including temporally variable jet features that rotated with the nucleus (*10*). The dust emission present in the CN and OH images was removed by assuming that the jet features in the filtered images contained only dust within 250 km of the nucleus (*11*). The subtraction is then performed using a scaled dust image that removes these jet features.

The surface brightnesses (B_s) of the dust, CN, and OH comae decreased with projected angular distance (ρ) from the nucleus in a manner similar to other comets (*12*). The radial fall-off in the dust coma displayed a typical surface brightness (B_{dust}) dependence of $B_{dust} \sim \rho^{-1}$ consistent with scattering of sunlight from optically thin dust with a number density (N_{dust}) distribution of $N_{dust} \propto r^{-2}$ around the nucleus (Fig. 2A) (*13*). This rate of decreasing intensity was the same for all angles from the sunward direction despite a clear asymmetry in dust production favoring the sunlit hemisphere. Both the CN (Fig. 2B) and OH images displayed radial surface brightness (B_{CN} and B_{OH}) distributions slower than ρ^{-1}, which is consistent with model simulations where these species are created over an extended region by photodissociation of parent molecules drifting away from the nucleus (*14*).

The density of dust in the inner coma was higher in the sunward-facing hemisphere (Fig. 2A), which agreed with the spatially filtered images showing discrete

W. M. Harris, Space Astronomy Laboratory, University of Wisconsin, 1150 University Avenue, Madison, WI 53706, USA.
M. R. Combi, Space Physics Research Laboratory, University of Michigan, 2455 Hayward Avenue, Ann Arbor, MI 48109-2143, USA.
R. K. Honeycutt, Department of Astronomy, Indiana University, Swain Hall West, Bloomington, IN 47405, USA.
B. E. A. Mueller, National Optical Astronomy Observatories, 950 North Cherry Avenue, Tucson, AZ 85719, USA.
F. Scherb, Department of Physics, University of Wisconsin, 1150 University Avenue, Madison, WI 53706, USA.

*To whom correspondence should be addressed. E-mail: wharris@sal.wisc.edu

jet regions only on the illuminated areas of the nucleus (*15*). Jet activity terminated nearly instantaneously after local sunset, and it appears that full illumination was required for dust production to occur. In contrast, neither the CN or OH images were asymmetric in the sunward direction; indeed, the CN difference images displayed a less pronounced, but distinct, antisunward brightening (Fig. 2B) (*16*). The orientation of the dust and ion tails of Hyakutake was nearly perpendicular to the line of sight on 26 March, providing a clear line of sight toward the nucleus that made it unlikely that projection effects could have caused these differences. Given that the inner coma volatiles are the source for the symmetric outer coma commonly observed from comets including Hyakutake (*17*), a spherical inner gas coma would be expected, but the problem of producing a symmetric coma with a nonspherical nuclear source distribution has not been successfully addressed (*18, 19*).

One possible explanation for the shape of the gas coma is that the nucleus of Hyakutake was surrounded by an extended cloud of volatile-rich particles with a gas production large enough to offset the sunward bias of the nucleus-centered source. Laboratory measurements have shown that icy particles will be driven off a comet nucleus by the evaporation of compounds more volatile than H_2O, with the diameter of the grains dependent on the size of the nucleus and its heliocentric distance (r_h) (*20*). The so-called icy grain halo (IGH) model (*20*) postulates that these liberated ice particles would be heated by sunlight and evaporate, contributing to the gas production of the comet. The ratio of surface area to mass of the icy particles is higher than the nucleus by the inverse ratio of their respective radii $(r_{grain}/r_{nucleus})^{-1}$, and, as they are heated by sunlight, they will outgas over time scales of seconds to hours. A continuously replenished supply of these particles could dominate gas production even when the instantaneous mass of the halo is $\ll$1% of the nucleus. Studies of the detectability of the icy particles and the size of a halo have shown the particles to have no obvious spectroscopic identifier, and that, unless they are composed of pure water ice, particles with diameters less than ~1 mm evaporate within 100 km of the nucleus at r_h of $\leq$1 AU (*21*). Because most halo particles evaporate very close to the nucleus, an IGH will subtend an angle of $\leq$1 arc sec at the Earth-comet distances typical of a closest approach (~1 AU), making it difficult to resolve from ground-based telescopes. To date, there have been no confirmed detections of a volatile-producing IGH around a comet nucleus, although they have been invoked to explain other observations (*22*).

If an IGH were present around Hyakutake, then it could have produced the observed characteristics of the gas and dust coma, because a distributed source will produce a more spherical coma than an asymmetrically active nucleus (*23*). It is also possible that evidence for an IGH was detected by the radar observations of Harmon *et al.* (*24*) on 25 March, which showed a slowly expanding distribution of approximately centimeter-size rubble in the inner coma with a total reflective cross section ~10 times greater than the nucleus. The diameter and drift rate (10 m/s) of this material agree with theoretical estimates for size and terminal velocity of the largest icy grains that could be accelerated to escape speeds by molecular drag from a 2-km (*24*) nucleus at 1 AU (*20*). Assuming that the particles had the same albedo as the nucleus, then the surface area of the halo would have been larger by the same factor of 10. The surface area and mass of a 0.01-m icy particle exceeds that of a 1000-m nucleus (*24*) by a factor of 10^5, and so the total mass in the halo necessary to provide the observed ratio in reflective area is only 0.001% of the nucleus. If the halo particles contained volatile material, and they were being continuously replenished, then their total gas production

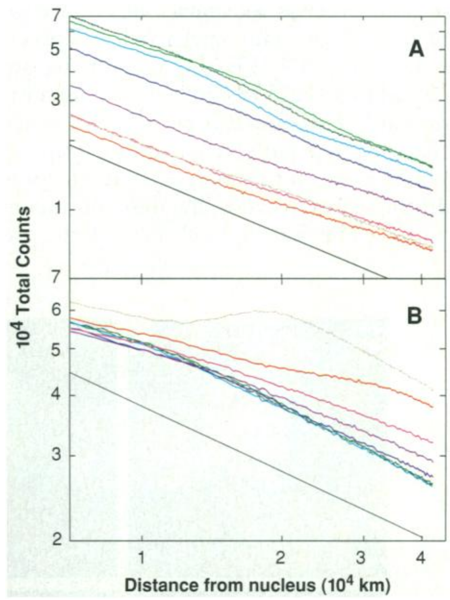

Fig. 2. The two plots show the radial intensity distributions for dust continuum (**A**) and CN (**B**) as a function of angular separation from the subsolar point of the comet. The different profiles are for angles of 0° (dark green), 20° (light green), 40° (aqua), 60° (blue), 80° (purple), 100° (pink), 120° (red), and 140° (gray). The black straight line on each plot is the best-fit radial profile ($\rho^{-0.85}$ for the dust and $\rho^{-0.45}$ for CN). The dust emission is more than twice as bright in the sunward side of the coma, reflecting the asymmetry in the source function on the nucleus. The CN profiles show no evidence of a sunward hemispheric asymmetry out to more than 80° from the subsolar point. Beyond this angle, the intensity of the coma begins to increase because of a combination of a possible antisunward asymmetry in CN production and the growing contribution of emission associated with the two arc structures (Fig. 1). The radial $\rho^{-0.45}$ fall-off rate for CN is also considerably slower than for the dust.

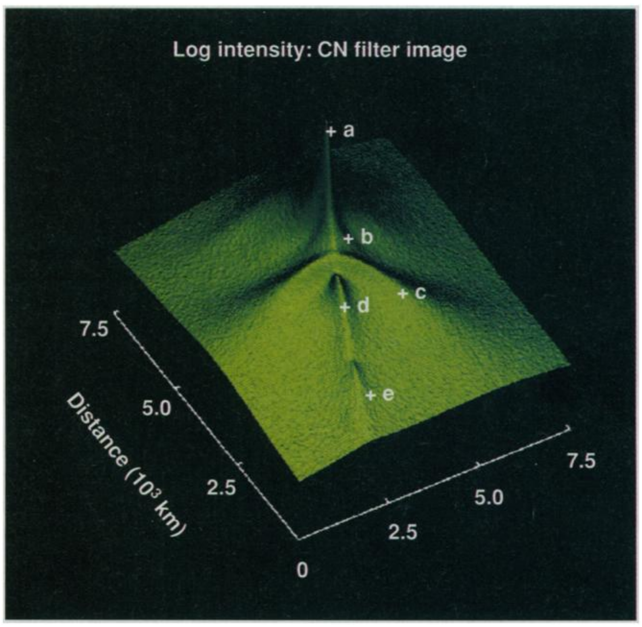

Fig. 1. This composite surface plot of four images taken over 15 min on 26 March 1996 with the CN isolation filter (*6*) shows the major features of the inner coma in both gas and dust. The image field of view is 8100 km on a side. To enhance the contrast of low surface brightness coma structures relative to the nucleus, we displayed the plot intensities logarithmically. The nucleus is located at the cross marked (a) with a jet feature visible toward its left. The arc-shaped emission features are located at (b) and (c), and the more prominent of the two can be seen crossing the comet-sun line in a parabolic shape, widening as it moves away from the nucleus. Trailing the large arc are two prominent extended condensations (d and e). The more distant condensation (e) was ~15% as bright as the inner one (d).

could have been comparable to or greater than the nucleus. A large halo gas source could also explain the high percentage (up to 100% depending on the nuclear diameter) of active surface area on Hyakutake's nucleus that would have been necessary to sustain the observed water production rate of $Q_{H_2O} > 10^{29}$ s^{-1} with a single source (*25*).

The other conspicuous components of the CN and OH images of 26 March were a transient bright arc-shaped emission feature that trailed the nucleus by ~1200 km and a smaller conical-shaped structure that trailed by ~200 km (Figs. 1 and 3). At its center the large arc was perpendicular to the line joining the nucleus and trailing debris, with a half-intensity width of 240 km and a surface brightness/pixel twice that of the background coma. With increasing distance from its apex the arc widened, decreased in contrast, and curved away from the comet-sun direction. It eventually approached a straight line directed radially away from the nucleus, and was detectable out to the edge of the 6.7 arc min image field. Between 6:38 and 11:09 UT, the apex of the arc moved from 1125 to 1365 (± 35) km antisunward of the nucleus at 10.9 ± 1.0 m/s (Fig. 4B). It maintained a constant separation from a condensation of debris that was drifting antisunward in the dust continuum images. The surface brightness of the arc and condensation were diminished on 27 March, with arc becoming undetectable by 29 March.

The closer conical feature appeared physically similar to the bright arc (Figs. 1 and 3), with its bright outer edges following a radial vector centered on the nucleus. It lacked the sharply defined apex of the larger feature, possibly due to the proximity of its crossing point to the nucleus. Like the brighter arc, the conical structure was associated with a nearby condensation that trailed the nucleus, but neither the conical structure nor the condensation showed evidence of tailward drift. Instead they maintained a fixed position relative to the nucleus, and remained detectable, although variable in brightness, over the entire period between 25 and 29 March.

The morphology of these features indicates that they each were produced by an interaction between gas flows from the nucleus and another region of locally intense outgassing in the tail. Because the structures of the large arc were always smaller than the local collisional mean free path (*26*), the gas molecule trajectories were ballistic, and hydrodynamic techniques cannot be used to model them. Instead, a gas-kinetic approach is required to understand the interactions (*27*). We studied the relationship of nonhydrodynamic gas flow interactions to the observed OH arc, using a direct simulation Monte Carlo (DSMC) gas-kinetic model for cometary atmospheres that follows the colliding trajectories of a swarm of many particles (*28*). The two-dimensional axisymmetric simulations employed a nucleus in interaction with combinations of secondary sources along the tail-axis of the comet, including point and extended sources. The model assumed a water-dominated comet containing 20% chemically inert species with a mean mass equal to that of a CO molecule. Full water photochemistry was included to track the distribution of H_2O, OH, H_2, O, and H, in addition to CO.

The DSMC simulations reproduced the intensity distribution in the OH arc using an interaction between the nucleus and a single extended secondary source (Fig. 3, D through F). The primary source in this simulation produced H_2O with a rate $Q_{H_2O} = 10^{29}$ s^{-1} plus 2×10^{28} s^{-1} with a particle mass equal to CO. The secondary source rate was $Q_{H_2O} = 2.3 \times 10^{28}$ ($\pm 10^{28}$) from a rotationally symmetric cylindrical distribution situated parallel to the comet-sun axis along a 200-km line centered 1250 km behind the nucleus, at the apex of the arc. Rotational symmetry was required to duplicate the observed symmetry of the arc and conical structures and results in a three-dimensional shape for the simulated arc similar to a paraboloid of rotation. The DSMC simulations were unable to reproduce an arc from a secondary point source, and its formation appears to be dependent on the presence of an initially cylindrical gas distribution (Fig. 3F) falling off perpendicular to the comet-sun line, a natural consequence of a linearly extended source. The high contrast areas of the simulated arc represent static regions of high gas density resulting from the intermingling of the two gas flows, not a standing shock. Because the mean free path for collisions increases with distance from the nucleus, the two simulated flows flow farther into one another, resulting in a widening of the arc with distance that is observed in the images.

The DSMC simulations of the arc structure were also useful for evaluating the characteristics of the associated visible debris condensation and its role in the production of the OH and CN arcs. The results from the simulations, along with the physical characteristics of the dust grains in the visible condensation itself, collectively indicate that the entrained grains were refractory particles that could not have been the true source of the arc. DSMC simulations reproduced the arc structures only when the secondary source was coincident with the apex of the arc,

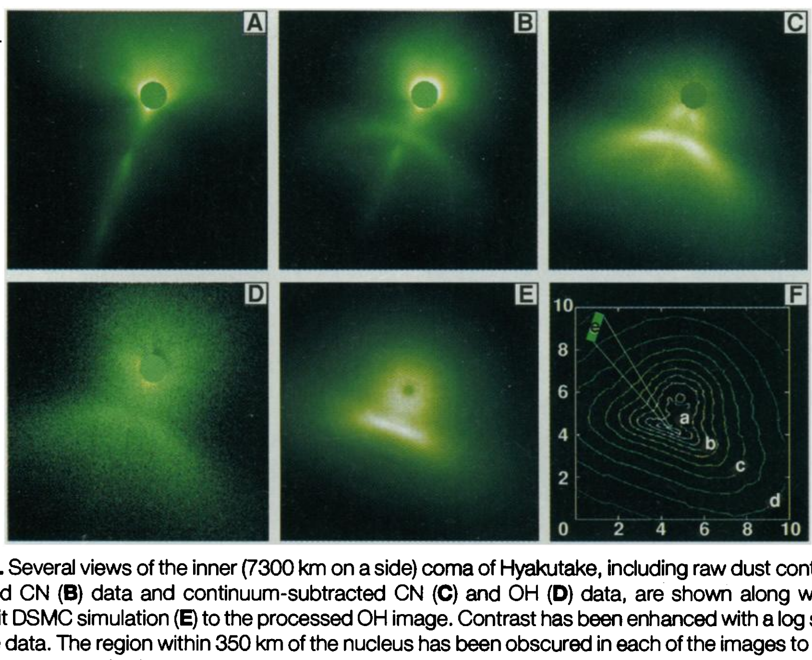

Fig. 3. Several views of the inner (7300 km on a side) coma of Hyakutake, including raw dust continuum (**A**) and CN (**B**) data and continuum-subtracted CN (**C**) and OH (**D**) data, are shown along with the best-fit DSMC simulation (**E**) to the processed OH image. Contrast has been enhanced with a log stretch on the data. The region within 350 km of the nucleus has been obscured in each of the images to further improve contrast in the coma and to cover artifacts of the subtraction. In addition to the images, a contour plot of the DSMC model (**F**) is provided to show the variations in OH column density produced by the best-fit DSMC simulation of the arc. Distances in (F) are in units of 1000 km and the individual contours give the log column density of OH. The labeled contours are (a) = 14.22, (b) = 14.15, (c) = 14.03, and (d) = 13.92. A representation of the model source (e) is displayed, in its correct orientation relative to the comet-sun line, in the upper left of the contour plot. The labeled source is enlarged by a factor of five for emphasis.

not 625 km antisunward of that point, where the observed visible condensation was centered. The model further indicated that, if the condensation were the secondary source of gas, then the CN and OH images would have shown a corresponding brightness peak at its location. Instead, the condensation was almost completely removed by the subtraction of dust from the CN images (Fig. 3C). Any evidence of it in the CN images is well within the uncertainty of our subtraction technique (*11*), and may not be real.

Measurements of the grain size distribution in the condensation region on 26 March were performed by Tozzi *et al.* (*29*) and gave an average value of ~300 μm. The lifetime of volatile-producing particles of this size at r_h = 1 AU against evaporation would be measured in minutes (*20, 21*) unless they were composed of pure H_2O ice [an improbable circumstance given the presence of the arc in CN, C_2 (*30*), and probably NH_2 (*31*) emissions]. This is too short an H_2O depletion time scale for the grains to still be outgassing after having drifted from near the nucleus to their location on 26 March; indeed, it is also too short for them to produce H_2O over the 6-hour duration of our observations. We also observed the condensation spreading out along the comet-sun axis on 26 March, with the measured center point of the region receding at approximately twice the rate of its leading edge (Fig. 4A). This is again inconsistent with the debris field surviving long enough to move 1500 km. Moreover, evolution in the linear extent of the source region should have caused corresponding changes in the shape and contrast of the arc that were not observed. A later observation of this condensation, at 4:40 UT on 29 March, showed it 4300 km from the nucleus. This distance corresponds to a constant drift rate of 10.3 m/s during these 3 days that is close to the tailward velocity of the arc on 26 March. A constant drift rate is not indicated by either the changing shape of the condensation or by the size distribution of the entrained grains, the smallest of which would have been accelerated by radiation pressure (*32*). The continued presence of the material on 29 March indicates replenishment of the dust grains by an unseen source of larger particles unaffected by radiation pressure.

The scenario that is most consistent with the available data is that there was a locally dense collection of evaporative grains with approximately centimeter-size or larger diameters located ~1250 km behind the nucleus on 26 March. Our estimate of the source particle size distribution is based on the longevity of the icy component of these grains, and on the similarity of the measured tailward drifts of the arc and condensation to the 10 m/s radial expansion velocity of the centimeter-size inner coma debris (*24*). Solar heating of the source particles would produce volatiles, which would flow away from the source region, and interact with outflowing gas from the nucleus-centered source to produce the arc. The DSMC simulations indicate that gas densities near the source particles were high enough for convective fluid behavior, but were not large enough to drag along dust grains. Therefore, although disintegration of these particles would also liberate many smaller dust grains in addition to gas, these would stay initially in the vicinity of the source particles rather than contributing to the development of a dust arc. This dust represents a good candidate for the visible condensation. A liberated 100-μm radius grain would have a ratio of surface area to mass 10^2 times greater than a 1-cm radius parent and a dust field composed of such grains would reflect more solar radiation than the source particles even if it represented only 1.0% of the total mass in the condensation. The rapid outgassing of water from these grains would push them tailward of the source region, where their remnant would be accelerated further back by radiation pressure (*32*) or outgassing of compounds other than H_2O. This would account for the observed separation of the arc and condensation and for the spreading out of the debris field, because the smaller grains would be accelerated to higher speeds by radiation. It also explains how a population of small grains could show no evidence of acceleration over 3 days, because the dust observed on any particular date would be a transitory population that was continuously replenished from the larger particles.

What is particularly compelling about the volatile-rich sources and their associated arc structures is their apparent stealthy nature. If the condensation was liberated dust and not the secondary source, then the source region must have had low contrast despite producing volatiles at a rate of 23% that of the nucleus. DSMC simulations of various trailing condensations with different viewing geometries indicated that the gas dynamic interactions observed from Hyakutake were detectable only under a narrow set of circumstances. Changes in the viewing geometry (*33*), the distance between the sources (*34*), the linear extent of the source region, or in the relative production rates of the two sources reduced the contrast of simulated structures associated with gas-producing condensations to the point where they became difficult to detect. An example of this from Hyakutake may have been present in the form of another condensation 3500 km behind the nucleus with a surface brightness 15% of

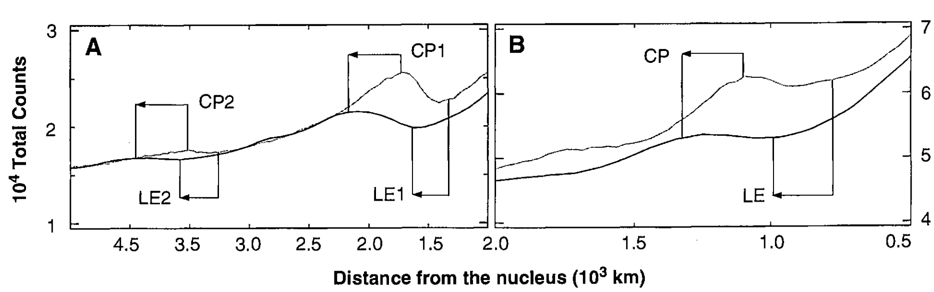

Fig. 4. The positions of the trailing condensations (**A**) and the bright arc (**B**) are shown for times near the end points (06:38 and 11:41 UT) of the observing sequence on 26 March using radial profiles taken 180° from the subsolar direction. Two characteristics are isolated here: the motion of the leading edges (LE) of these structures and the motion of their center points (CP). The center points were determined by subtracting a linear fit to points on either side of the condensations, and then using a feature-summing algorithm to determine the center of the remainder. The leading-edge positions were obtained by inverting the radial profiles and using a similar linear-fit subtraction and feature sum technique to identify the inflection point of the curve leading into the arc or condensation. Over the 5 hours between these observations, the arc center point moved ΔCP = 184 ± 18 km, corresponding to a velocity of 10.9 ± 1.0 m/s, while its leading edge moved ΔLE = 169 ± 18 km, corresponding to 10.0 ± 1.0 m/s. The velocities of the leading edges of the closer (LE1) and more distant (LE2) condensations were similar to the arc (ΔLE1 = 200 ± 18 km, velocity = 11.1 ± 1.0 m/s, and ΔLE2 = 230 ± 27 km, velocity = 12.6 ± 1.5 m/s); however, the velocities of the center points, CP1 and CP2, were nearly twice that of the arc (ΔCP1 = 354 ± 18, velocity = 19.4 ± 1.0 m/s, and ΔCP2 = 340 ± 27 km, velocity = 18.5 ± 1.5 m/s). The differential in the CP and LE velocities indicates a reshaping of the debris distribution along the tail axis of the comet, consistent with the effect of radiation pressure acting differentially on grains of different sizes acting on a distributed source. No broadening of the arc was detected, as its center point retreated from the nucleus at the same rate as its leading edge.

the brighter one (Fig. 1). This feature appeared physically similar to (29), and was moving and spreading out at approximately the same rate as its brighter counterpart (Fig. 4A). As with the larger condensation, its morphology indicated continual replenishment of dust grains from the evaporation of larger particles, but in this case there was no evidence for any associated gas dynamical structure. The lack of a detectable arc associated with possible outgassing from this condensation, along with the disappearance of the bright arc at a similar nuclear distance on 29 March, both agree with the predictions of the DSMC model (35), and suggest the possibility that compact sources of volatile production (5 to 100% of the nucleus) could be common, but rarely observable, components of a comet coma. The only record that these sources existed would be the depleted dust grains produced by the disintegration of source particles, and this suggests a method for identifying candidate regions in other comets with less favorable viewing conditions than Hyakutake.

REFERENCES AND NOTES

1. All ephemeris data were supplied by D. Yeomans using the Naval Ancillary Information Facility program.
2. S. M. Larson, Z. Sekanina, D. Levy, S. Tapia, M. Senay, *Astron. Astrophys.* **187**, 639 (1987).
3. H. U. Keller *et al.*, *ibid.*, p. 807.
4. E. P. Mazets *et al.*, *ibid.*, p. 699.
5. The WIYN [Wisconsin, Indiana, Yale, NOAO (National Optical Astronomical Observatories)] observatory is a 3.5-m telescope located at the Kitt Peak National Observatory (east longitude = −111°36.0′, latitude 31°57.8′, and altitude of 2120 m). The telescope employs active optical techniques to achieve ground-based seeing as good as 0.4″.
6. On 26 March 1996, we used four filters to isolate specific comet spectral features including OH [wavelength of 3080 Å; full width at half maximum (FWHM), 20 Å], CN (3919 Å; FWHM, 199 Å), and blue dust continuum (4875 Å; FWHM, 75 Å) emissions. We also obtained images with a broad-band Harris R filter (6461 Å; FWHM, 1526 Å), which permitted 0.1 s exposure times that made the best use of available seeing and the limited nonsidereal tracking capabilities of the WIYN. At the time of the Hyakutake apparition, the WIYN observatory was not equipped with a set of the standard comet filters. We were able to find acceptable substitutes; however, only the OH bandpass may be considered free of molecular emission features out of the desired bandpass (for example, some C_3 contamination was present in the CN filter bandpass).
7. D. G. Schleicher, R. L. Millis, D. J. Osip, S. M. Lederer, *Bull. Am. Astron. Soc.* **28**, 1089 (1996).
8. See W. Huggins [*C.R. Acad. Sci.* **10**, 26 (1881)] for discussion of the CN band and C. Fehrenbach and C. Arpigny [*ibid.* **277B**, 569 (1973)] for the OH band.
9. Standard processing for WIYN images includes subtraction of instrument bias and division by a flat field taken the same day as the observation. Images taken before September 1996 include an additional processing stage to account for nonlinearity at very low light levels that were present in the WIYN imager charge-coupled device at the time of these observations. The correction algorithms were supplied courtesy of T. Von Hippel (University of Wisconsin) and D. Silva (NOAO).
10. To emphasize small-scale spatial structure, each image was divided by a smoothed version of itself. The smoothed image was created by the application of a 4 arc sec (20 pixel) median filter. The remainder after this division consists of detailed features of the near-nuclear region, with a spatial scale smaller than the filter, that are difficult to detect above the bright background of the coma.
11. To correctly subtract dust from CN requires knowledge of the ratio of dust continuum emission in the dust filter band pass to that in the CN filter bandpass, and the contribution of emissions from other molecular species, aside from CN, that contribute to the total signal in either filter. It is also necessary to know the atmospheric extinction for each image used in the subtraction. From this, it is possible to perform an exact separation of dust and gas emission with the relation $I(gas) = I(gas/dust) - A * I(dust)$, where A is a constant that accounts for the ratio of dust emission in the two bandpasses. We were unable to use this method, because our observations were conducted under nonphotometric conditions, and we had no information about either the relative amount of dust emission or about the contribution of molecular species, such as C_3, C_2, or CO^+, in our different approximations to the standard bandpasses used in comet observations. Our method of assuming that the projected dust jets within 250 km of the nucleus were devoid of CN or OH emission gives consistent results, but it can lead to an oversubtraction of the dust in the areas where gas and dust emission regions overlap. The importance of the oversubtraction for the shape and intensity of the arc features was minimal, because these structures are present only in the CN or OH images. We examined the effect of subtracting different percentages (±25% from best fit) of the dust emission from gas images, and, whereas the detailed structures in gas emission in the difference image are highly dependent on the accuracy of the subtraction, it did not affect the general differences in spherical symmetry between gas and dust discussed here.
12. D. C. Jewitt and K. J. Meech, *Astrophys. J.* **317**, 992 (1987).
13. This represents the most simple case for describing the radial surface brightness B_s at any projected angular distance ρ from the nucleus. It assumes an optically thin coma where the grains move at a constant velocity relative to the nucleus, are produced and lost at the same rate, and do not evolve in their size distribution or scattering efficiency. Under these conditions, the number density of the grains $N(r)$ (where r is the radial distance to the nucleus at any point along a line of sight l) will decrease following an inverse square relation $N(r) \propto r^{-2}$, and the equation for the optically thin surface brightness along any line of sight $B_s(\rho) = S\int N\,dl$ (where S is a constant related to size and scattering of the grains) integrates to $B_s(\rho) = S'/\rho$ (where S' is again a constant). Despite the gross simplifications implied in this case, most comets deviate only slightly from a photometric angular profile of $B_s(\rho) \propto \rho^{-1}$ over large spatial scales.
14. M. R. Combi and A. H. Delsemme, *Astrophys. J.* **237**, 1026 (1980).
15. W. M. Harris, F. Scherb, M. R. Combi, B. E. A. Mueller, *Bull. Am. Astron. Soc.* **28**, 1088 (1996).
16. At angles $\gtrsim 100°$ from the sunward direction, an asymmetry begins to assert itself in the volatile radial distribution that favors the antisunward hemisphere, with the degree of asymmetry greatest at larger distances from the nucleus. Rather than reflecting a deviation from radial symmetry in the volatile source distribution, the additional signal appears to be from an unrelated local density enhancement associated with outgassing material in the tail. Whereas this feature becomes dominant at large angles from the sunward direction, it does not contribute at angles smaller than ~100°, and can not explain the difference in overall symmetry between gas and dust.
17. Wide-field observations of the radial distribution of neutral oxygen [OI] (6300 Å) emission from Hyakutake with the narrow band Wisconsin H-alpha Mapper (WhαM) instrument at the Pine Bluff Observatory showed nearly perfect spherical symmetry in the coma out to more than 0.5° (L. M. Haffner, personal communication).
18. Y. Kitamura, *Icarus* **66**, 241 (1986).
19. A. Korosmezy and T. I. Gombosi, *ibid.* **84**, 118 (1990).
20. A. H. Delsemme and A. Wenger, *Planet. Space Sci.* **18**, 709 (1970).
21. T. Mukai, S. Mukai, H. Fechtig, E. Grün, R. H. Giese, *Adv. Space Res.* **5**, 339 (1985); M. S. Hanner, *Icarus* **47**, 342 (1981).
22. See A. H. Delsemme and D. C. Miller [*Planet. Space Sci.* **19**, 1259 (1971)] for discussion of C/1960-II Burnham; M. F. A'Hearn, C. H. Thurber, and R. L. Millis [*Astron. J.* **82**, 518 (1977)], M. F. A'Hearn and J. J. Cowan [*Moon Planets* **23**, 41 (1980)], and K. Saito, S. Isobe, N. Nishioka, and T. Ishii [*Icarus* **41**, 351 (1981)] for C/1975n West; and R. L. Newburn, J. F. Bell, and T. B. McCord [*Astron. J.* **86**, 469 (1981)] for P/Ashbrook-Jackson.
23. Solar heating rapidly increases the temperature of the icy grains until they reach equilibrium or become hot enough to vaporize and break up. This is why larger, more reflective grains last longer than small dirty ones. Once a grain reaches its critical temperature, it begins to evaporate with greater spherical symmetry than the nucleus. When integrated over an entire halo of icy grains, this process produces a more spherically symmetric coma for a comet than a nucleus source, even if the IGH is itself nonspherical. This mechanism also accounts for the lack of a spherically symmetric dust halo. The gas liberated from the icy grains will expand adiabatically away at ~0.8 km/s (or roughly twice the thermal speed of water at the vaporization temperature of 190 K); however, there is not enough molecular drag near the smaller grains to accelerate any dust that is produced. The dust will therefore remain in the vicinity of its parent grain until accelerated antisunward into the tail by radiation pressure rather than out into the spherical coma.
24. J. K. Harmon *et al.*, *Bull. Am. Astron. Soc.* **28**, 1195 (1996).
25. M. F. A'Hearn, *Proceedings of the 1996 Asteroid, Comet, and Meteor Conference*, in press.
26. Fluid theory predicts a contact discontinuity between the interacting flows, but there will be a finite width to a ballistic interaction region limited by the collisional mean free path. For a water production of $Q_{H_2O} = 10^{29}$ s^{-1}, the collisional mean free path with distance from the nucleus is given by $\lambda_{col} = (n\sigma)^{-1}$, where $n = Q_{H_2O}/(4\pi r^2 v)$ is the gas density (using $\sigma \sim 3 \times 10^{-15}$ cm^2 and $v \sim 0.8$ km/s as estimates for the collision cross section and radial flow velocity). This corresponds to a mean free path of 335 km (compared with the measured 240 km of the arc) at the $r = 1000$ km distance of the arc center point, and to 14,200 km at $r = 6500$ km. The scale of these values is consistent with the observed central width and widening of the large arc.
27. The gas-kinetic model may not be the best approach for the smaller arc, because it emanates from a region of the coma where the mean free path (for $r = 200$ km, $\lambda_{col} = 13$ km) is smaller than the width of the observed structures. A hydrodynamic model solution is indicated under these conditions.
28. M. R. Combi, *Icarus* **123**, 207 (1996).
29. G. P. Tozzi, G. B. Field, E. Mannucci, P. Patriarchi, R. M. Stanga, *Bull. Am. Astron. Soc.* **28**, 1089 (1996); G. P. Tozzi, personal communication.
30. C. Laffont, P. Rousselot, J. Clairemidi, G. Moreels, *ibid.*, p. 926.
31. Because our choice of bandpass for the dust continuum filter was limited, we used filters that contained signal from C_2 and NH_2 contamination in addition to dust. Similarly, the Harris R filter was chosen for its broad-band high throughput as opposed to spectral purity, and both H_2O^+ and NH_2 emissions are present. The presence of small amounts of emission from the arc features in these filters is a possible detection of C_2 and NH_2 arcs in addition to CN and OH. Observations on 27 March with a narrow bandpass H_2O^+ filter showed no

evidence of either feature, and this argues against the possibility that either an ion or dust arc was present.

32. Dust and small fragments are subject to gravity, radiation pressure, and outgassing. The gravitational force $F_G = GM_\odot[4\pi a^3\rho/3]r_h^{-2}$ is counterbalanced by radiation pressure $F_R = L_\odot Q_{pr} a^2/[4r_h^2 c]$ and a less defined outgassing force $F_J = mv_g Q_{H_2O}$, where $L_\odot$ and $M_\odot$ are the solar mass and luminosity, a is the radius of the particle, r_h is the heliocentric distance, Q_{pr} is the radiation interaction efficiency, Q_{H_2O} is the water production rate, m is the mass per outgassed molecule, c is the speed of light, and v_g is the vectored average velocity of outgassed volatiles (0 m/s for spherical symmetry). The motion of particles larger than several millimeters is dominated by gravity, and they tend to stay co-orbital with the nucleus until they get close to the Sun, where Q_{H_2O} increases to the point that outgassing becomes a significant force.
33. Successive runs of the DSMC model indicated that the contrast of these interaction regions is a maximum for a sun-comet-Earth (SCE) angle near 90°, and that visibility drops rapidly away from this geometry. The arc seen on 26 March would have been undetectable for viewing geometries of 45° > SCE > 135°.
34. As discussed (*26*), the dimensions of the contact discontinuity between the two flows is dependent on the local collisional mean free path, which increases as r^2 away from the nucleus. As a result, volatile sources close to the nucleus will generate interaction regions with more compact dimensions than more distant sources.
35. An arc associated with the secondary condensation at 3500 km would have a width at its apex of more than 3000 km, with its surface brightness reduced by a factor of 12 relative to what it would have been at the location of the bright arc. Assuming that the brightness of the visible dust condensation accurately mirrors gas production (15%), then this source would produce an arc with 1% of the surface brightness of the brighter source. This would not have been detectable in our images.
36. We acknowledge the generous contribution of time and effort by the staff at the WIYN observatory and, in particular, D. Sawyer for supporting such a large unexpected observing program. We also thank J. Percival for work in modifying the WIYN control system to permit tracking of a moving source, F. Roesler for donation of an OH filter, D. J. Lien for many useful conversations on the topic of halo debris, and J. Wisniewski for assisting in the reduction of the images. Supported by the WIYN consortium universities and NOAO, by NASA grants NAGW-3319, W18963, and NAG5-647 to the University of Wisconsin, and by NASA grant NASW-1907 to the University of Michigan.

4 March 1997; accepted 30 May 1997

Failure of Parturition in Mice Lacking the Prostaglandin F Receptor

Yukihiko Sugimoto, Atsushi Yamasaki, Eri Segi, Kazuhito Tsuboi, Yoshiya Aze, Tatsuya Nishimura, Hiroji Oida, Nobuaki Yoshida, Takashi Tanaka, Masato Katsuyama, Ken-yuh Hasumoto, Takahiko Murata, Masakazu Hirata, Fumitaka Ushikubi, Manabu Negishi, Atsushi Ichikawa,* Shuh Narumiya

Mice lacking the gene encoding the receptor for prostaglandin $F_{2\alpha}$ (FP) developed normally but were unable to deliver normal fetuses at term. Although these FP-deficient mice showed no abnormality in the estrous cycle, ovulation, fertilization, or implantation, they did not respond to exogenous oxytocin because of the lack of induction of oxytocin receptor (a proposed triggering event in parturition), and they did not show the normal decline of serum progesterone concentrations that precedes parturition. Ovariectomy at day 19 of pregnancy restored induction of the oxytocin receptor and permitted successful delivery in the FP-deficient mice. These results indicate that parturition is initiated when prostaglandin $F_{2\alpha}$ interacts with FP in ovarian luteal cells of the pregnant mice to induce luteolysis.

Prostaglandins (PGs) mediate various physiological processes such as fever generation and inflammation (*1*). Aspirin and related drugs act through inhibition of PG biosynthesis. The prostaglandin $PGF_{2\alpha}$ is implicated in reproductive functions such as ovulation, luteolysis, and parturition. Actions of $PGF_{2\alpha}$ are mediated by the PGF receptor (FP), which is a heterotrimeric guanosine triphosphate–binding protein (G protein)–coupled rhodopsin-type receptor specific to this PG (*2*). To examine the physiological function of $PGF_{2\alpha}$, we disrupted the gene encoding FP in mice by homologous recombination.

A targeting vector was constructed in which the coding region of the second exon of the FP gene could be replaced with the β-galactosidase and neomycin resistance genes (Fig. 1A) (*3*). Heterozygous mice (−/+), when crossed, yielded homozygotes (−/−) (Fig. 1B) with a frequency of 25.6% (n = 262), indicating that mice lacking FP develop normally. X-Gal staining of β-galactosidase in homozygous mice showed that the targeted allele was expressed in the corpora lutea in ovaries (Fig. 1C) (*4*), as is FP (*2*). Disruption of the FP gene was verified in the ovary by both Northern (RNA) blot analysis and radioligand binding assay (*5*). FP mRNA expression was reduced in heterozygous mice and absent in homozygous mice (Fig. 1D). Specific $[^3H]PGF_{2\alpha}$ binding in a crude membrane preparation of the ovary (mean ± SEM, n = 8) was 121.3 ± 4.8 fmol per milligram of protein, 38.7 ± 1.6 fmol/mg, and below the limit for detection for wild-type, heterozygous, and homozygous mice, respectively. Homozygous FP mice also lacked the normal ileac contractile response to $PGF_{2\alpha}$ (Fig. 1E).

Homozygous mutant mice were healthy. No gross abnormalities were found in mutant animals in their general behavior, general appearance, or tissue histology, or from biochemical and hematological examination. Homozygous males were normal in their reproductive ability. Although $PGF_{2\alpha}$ is critical to luteal regression in ovine and sow (*6*) and FP is expressed in the corpora lutea of mice during the normal estrous cycle (*2*), no change was found in the estrous cycle in homozygous or heterozygous FP females compared with wild-type mice (Table 1). The homozygous females were also able to become pregnant. The number of corpora lutea and implants in the uterus

Y. Sugimoto, A. Yamasaki, E. Segi, K. Tsuboi, M. Katsuyama, K. Hasumoto, M. Negishi, A. Ichikawa, Department of Physiological Chemistry, Faculty of Pharmaceutical Sciences, Kyoto University, Kyoto 606, Japan.
Y. Aze, T. Nishimura, H. Oida, Fukui Research Institute, Ono Pharmaceutical Company, Limited, Fukui 913, Japan.
N. Yoshida and T. Tanaka, Division of Molecular and Cellular Immunology, Research Institute, Osaka Medical Center for Maternal and Child Health, Osaka 590-02, Japan.
T. Murata, M. Hirata, F. Ushikubi, S. Narumiya, Department of Pharmacology, Faculty of Medicine, Kyoto University, Kyoto 606, Japan.

*To whom correspondence should be addressed.

Table 1. Estrous cycle, ovulation, and fertilization in wild-type and mutant mice. Female mice of either genotype were mated with wild-type males and examined at day 19 of pregnancy. Data are mean ± SEM.

Variable	Genotype		
	+/+	+/−	−/−
Estrous cycle, days	5.1 ± 0.35 (n = 19)	5.4 ± 0.37 (n = 14)	5.0 ± 0.32 (n = 17)
Number of corpora lutea	9.0 ± 0.62 (n = 6)	9.2 ± 0.72 (n = 5)	9.4 ± 0.45 (n = 7)
Number of implants	7.9 ± 0.96 (n = 6)	8.4 ± 1.10 (n = 5)	8.8 ± 0.51 (n = 7)